Acta Astronautica 216 (2024) 488–503

Contents lists available at ScienceDirect

Acta Astronautica

journal homepage: www.elsevier.com/locate/actaastro

Unsteady interaction and dynamic stability analysis of a two-stage-to-orbit vehicle during transverse stage separation

Yue Wang [a,b], Yunpeng Wang [a,b,*]

[a] State Key Laboratory of High Temperature Gas Dynamics, Institute of Mechanics, Chinese Academy of Sciences, Beijing, 100190, China
[b] School of Engineering Science, University of Chinese Academy of Sciences, Beijing, 100049, China

ARTICLE INFO

Keywords:
Multibody separation
Hypersonic
Dynamic stability
Center of pressure
Aerodynamic interaction
Numerical simulation

ABSTRACT

Hypersonic stage separation is a significant process for the future two-stage-to-orbit (TSTO) vehicle. Strong and complex interstage aerodynamic interference may result in drastic aerodynamic forces and moments, potentially conflicting with the safe separation. Therefore, the dynamic stability of the vehicle during separation is critical to aerospace safety. In this study, numerical analysis of a hypersonic flow with $Ma = 6.7$ past a parallel-staged TSTO vehicle during stage separation is performed by laminar flow simulations. The TSTO vehicle consists of a wave-rider and a spaceplane as booster and orbiter, respectively. Considering the different centers of gravity for the orbiter during separation, the longitudinal dynamic stability of the orbiter is analyzed based on the dynamic characteristic of the center of pressure (CoP) in different cases. The dynamic separation behavior, aerodynamic characteristics, and typical flowfield patterns are clarified. Moreover, the derivative of CoP to time is proposed and analyzed in detail, which serves as an indicator to determine the dynamic stability and the safe stage separation. A safety separation judgment criterion is also proposed based on the CoP dynamic characteristics for the TSTO vehicle, and the mechanism of CoP variations associated with the unsteady aerodynamic interference during stage separation is revealed.

1. Introduction

The horizontal take-off and landing two-stage-to-orbit (TSTO) reusable launch vehicle is a promising airline space transportation system and has received much attention [1–3]. The parallel-staged TSTO vehicle may comprise the booster with an airbreathing combined engine and the orbiter with a rocket engine[3], and the stage separation typically occurs under hypersonic conditions. For example, the Saenger TSTO concept has a staging Mach number of 6.7 [1]. Thus, the high-speed flow past a TSTO vehicle (e.g., a two-body system [4–8]) may be associated with shock wave-shock wave interaction (SSI) and shock wave-boundary layer interaction (SBLI), as well as flow separation [9–14]. In terms of high-speed complex interactions, advanced applications (e.g., the interaction between the shock wave and transverse jets in supersonic flow) have been investigated. Gerdroodbary et al. [15–19] studied the fundamental flow physics of the interaction between fuel jets and air jets in a supersonic transverse flow. The complex features of the multi-jets in supersonic flow were analyzed, and their significant effects on the penetration of hydrogen jets were clarified. Moreover, the effects of jet number, total pressure ratio, inflow Mach numbers, etc., on fuel and air mixing performance were discussed in several studies. Based on these studies, the unsteady complex interaction is important in high-speed flow, especially for TSTO stage separation applications involving multi-body moving. The strong unsteady flow effect of aerodynamic interference coupled with the motion of the vehicle body increases the risk and difficulty of the stage separation of the TSTO vehicle. Therefore, stage separation is one of the critical problems for TSTO vehicles and multibody separation in a hypersonic regime.

Parallel-staged TSTO may have different separation schemes. Wang et al. [20] proposed two candidate schemes, i.e., longitudinal and transverse stage separation, and distinguished between these two schemes. Recently, longitudinal stage separation has been investigated by computational fluid dynamics (CFD) simulations [21,22] and free-flight experiments in the JF-12 shock tunnel [23,24]. Moreover, Wang et al. [25] analyzed the CFD and free-flight test results of unsteady interactions during longitudinal stage separation for parallel-staged TSTO vehicles. The results demonstrated the feasibility and reliability of the longitudinal stage separation scheme, which reduced the interstage aerodynamic interaction. In addition, transverse stage separation has been a research hotspot due to its complex high-speed flow

* Corresponding author. State Key Laboratory of High-temperature Gas Dynamics, Institute of Mechanics, Chinese Academy of Sciences, Beijing, 100190, China.
E-mail address: wangyunpeng@imech.ac.cn (Y. Wang).

https://doi.org/10.1016/j.actaastro.2024.01.002
Received 18 September 2023; Received in revised form 29 December 2023; Accepted 3 January 2024
Available online 12 January 2024
0094-5765/© 2024 IAA. Published by Elsevier Ltd. All rights reserved.

phenomena involving unsteady interaction mechanisms and aerodynamics [26]. Decker [26] conducted a wind tunnel investigation using a simple TSTO configuration to examine the aerodynamic interference effects. Static measurements of the effects of the interstage vertical gap and relative incidence angle were performed at Mach 3 and 6. Bordelon et al. [27] carried out a wind tunnel test on a TSTO model. The measurement results showed that the TSTO vehicle was statically unstable due to strong shock interactions at several relative separation positions. Ozawa et al. [28] investigated the effects of the interstage gap in a simple configuration on the aerodynamic interference at Mach 8.1 through experiments. The results showed that the flow pattern would be unsteady with shock oscillation under a certain interstage gap. To reduce interstage aerodynamic interaction, Uematsu et al. [29] carried out aerodynamic interaction experiments with different cross-sections for simplified TSTO configuration. The results showed that the triangular cross-section of the booster was effective in minimizing the shock wave interaction. In addition, Peng et al. [9] and Liao et al. [10] found strong aerodynamic interference and associated peak air and thermal loads in the parallel-staged TSTO configurations. Cheng et al. [30] performed numerical simulations of the aerothermodynamics of the TSTO. The results indicate that the complex interstage shock wave interaction features contribute to the significant increase in aerothermal loads at shock reflection positions. Furthermore, Wang et al. [31] numerically simulated the dynamic stage separation for a simple TSTO configuration and analyzed the effects of the incidence angle on stage separation. The results showed that aerodynamic interference becomes stronger and more complex as the incidence angle increases. Since Wang et al. [22] proposed the spiked model for parallel-staged TSTO vehicles, Liao et al. [32] investigated the transverse stage separation for spiked TSTO vehicles and analyzed the flowfield structure variation with increasing angle of attack. The results showed that the aerospike reduced the aerodynamic interaction between stages and lowered the drag. Cvrlje [33] investigated the separation maneuver of an idealized TSTO vehicle aerodynamically by CFD. The unsteady flowfields arising from translatory motion were calculated. The results showed that the separation is dominated by reflected shocks, and the unsteadiness has a significant effect on the air loads. Cvrlje et al. [34] numerically investigated the influence of yaw and roll harmonic oscillations on the entire flowfield and resulting air loads. They demonstrated that quasi-steady values do not accurately approximate the unsteady behavior even at low reduced frequencies. When stronger aerodynamic interference occurs between stages, the unsteady effects tend to be more significant. Moelyadi et al. [35,36] performed steady and unsteady simulations for stage separation aerodynamics of the TSTO system. The flow patterns demonstrate strong interference effects from incident, reflected, and expansion waves. Moreover, since the aerodynamics of stages significantly change at the beginning of the separation maneuver, the unsteady characteristics must be carefully considered. Wang et al. [13] and Liu et al. [37] demonstrated that the two stages might suffer from the risk of stage collision and separation failure due to unsteady and strong interference aerodynamics. Particularly, the pitching moment of the orbiter is sensitive to the separation parameters during stage separation, significantly affecting the TSTO separation.

The above studies on the transverse stage separation for the TSTO vehicle have revealed the significant influence of the unsteady and strong aerodynamic interference on the aerodynamics of the stage, which directly determines the separation process. In particular, the balance of moments is essential for a safe separation maneuver. The unsteady aerodynamic interference may lead to drastic variations in the moment balance, making it necessary to carefully consider the separating stability of the vehicle. Moreover, several studies investigated the unsteadiness by the harmonic oscillation of the orbiter at a certain position. The dynamic stability issues of TSTO vehicles during stage separation were rarely reported. There were few published studies on the dynamic stability of the aerospace vehicle under strong disturbance (i.e., strong aerodynamic interference), and no corresponding judgment criteria associated with dynamic separating stability for TSTO separation were proposed. In this study, a series of CFD simulations were performed to realize TSTO stage separation by changing the center of gravity (CoG) of the orbiter. The longitudinal stability of the orbiter was analyzed by investigating the variations of the center of pressure (CoP) and its derivatives for different cases. The remaining sections of this paper are organized as follows: Section 2 introduces the size and details of the parallel-staged TSTO model. Based on the TSTO model, the unsteady hypersonic flowfields during stage separation are simulated for different CoG cases. Section 3 describes the governing equations, numerical methods, and boundary conditions. A computational overset grid for TSTO stage separation is presented, and verification of the computational grid and the time step the validations for numerical methods are also performed. Section 4 presents detailed results and discussion, including dynamic separation behavior and unsteady aerodynamics, interaction mechanism with the changing of the flow structures and wall pressure, and aerodynamics. The CoP characteristics involved in longitudinal dynamic stability, the derivative of CoP to time, and the linear stability method are analyzed in detail. Several judgment criteria for outcome-based safety conditions and TSTO vehicle CoP-based safety separation are specified. Finally, the conclusions of this study are presented in Section 5.

2. TSTO model

The parallel-staged TSTO model for the numerical simulation consists of a wave rider and a spaceplane as the booster and the orbiter, respectively [21–25]. The booster is designed as a wide-speed range vehicle with a deformable wing and twin vertical tails based on a conically derived wave-rider. The orbiter is designed as a large swept wing body with a vertical tail. Fig. 1 presents the size of the TSTO model with the origin of the coordinate system on the nose of the booster. The leading edge of the booster and the orbiter is blunted with a blunt radius of 1 mm. The length and span of the booster are $l_b = 1$ m and $w_b = 0.55$ m, respectively, and its CoG is located at (0.738, −0.05, 0) m, which is about 73.8% of its length. The length and span of the orbiter are $l_o = 0.4$ m and $w_o = 0.186$ m, respectively. The CoG of the orbiter is only one independent variable (l_{CoG}/l_o = 0.65, 0.675, 0.687, 0.70, 0.71, 0.725, 0.75, 0.80), and the CoG of the orbiter offsets from the lower surface is $h_{CoG}/d_o = 0.32$. The minimum interstage clearance is $h/l_b = 0.015$, and the initial incidence angle between the orbiter and booster is 8°. The angle of attack of the TSTO vehicle is zero. The non-dimensional mass of

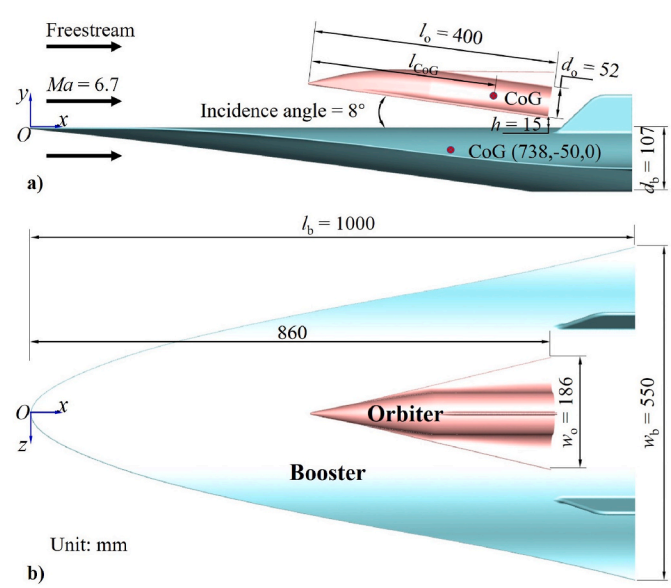

Fig. 1. The overall size of the scaled TSTO model.

the orbiter is $m_o/\rho_\infty l_o^3 = 2660$, and the moments of inertia are $I_{xx}/\rho_\infty \cdot l_o^5 = 18$, $I_{yy}/\rho_\infty \cdot l_o^5 = 165$, and $I_{zz}/\rho_\infty \cdot l_o^5 = 154$, with $\rho_\infty = 0.0074$ kg m^{-3} indicating freestream density. Moreover, the booster is assumed to be fixed in the simulation, while the orbiter is separated freely from the booster. The orbiter is governed by the six degrees of freedom (6-DOF) motion equations under the aerodynamic forces, moments, and gravity force. The reference point for the moments is located on the CoG. In the simulations, the mechanical connection and separation of the unlocking device between the two stages and the vehicle engine are omitted.

3. Numerical methods and validations

3.1. Computational methods

The Navier-Stokes (N–S) and the 6-DOF rigid body dynamics equations are solved for the unsteady flowfield during the TSTO stage separation process. The unsteady three-dimensional (3-D) N–S equations employed for the simulation are given by:

$$\frac{\partial}{\partial t}\iiint_{\Omega} \boldsymbol{W} d\Omega + \oiint_{\partial\Omega} (\boldsymbol{F}_c - \boldsymbol{F}_v) d\boldsymbol{S} = 0 \tag{1}$$

where $\boldsymbol{W}$ indicates conservative variables; $\boldsymbol{F}_c$ represents the vectors of convective fluxes; and $\boldsymbol{F}_v$ denotes viscous fluxes. These parameters can be expressed as:

$$\boldsymbol{W} = \begin{pmatrix} \rho \\ \rho u \\ \rho v \\ \rho w \\ \rho E \end{pmatrix}, \boldsymbol{F}_c = \begin{pmatrix} \rho \boldsymbol{V_r} \\ \rho u \boldsymbol{V}_r + n_x p \\ \rho v \boldsymbol{V_r} + n_y p \\ \rho w \boldsymbol{V_r} + n_z p \\ \rho H \boldsymbol{V}_r + \boldsymbol{V_g} p \end{pmatrix}, \boldsymbol{F}_v = \begin{pmatrix} 0 \\ n_x \tau_{xx} + n_y \tau_{xy} + n_z \tau_{xz} \\ n_x \tau_{yx} + n_y \tau_{yy} + n_z \tau_{yz} \\ n_x \tau_{zx} + n_y \tau_{zy} + n_z \tau_{zz} \\ n_x \Theta_x + n_y \Theta_y + n_z \Theta_z \end{pmatrix}, \tag{2}$$

where ρ is the density; u, v, and w are the velocity components in the x, y, and z directions, respectively; p denotes the pressure; E and H are the total energy and total enthalpy per unit mass, respectively. Moreover, $p = (\gamma\text{-}1)[\rho E - 1/2\rho(u^2 + v^2 + w^2)]$ and $H = E + p/\rho$, where γ is the specific heat ratio; τ_{ij} is the component of viscous stress; Θ_x, Θ_y, and Θ_z represent the heat conduction; n_x, n_y, and n_z are the components of unit outward-facing normal vector; $\boldsymbol{V_r}$ represents the contravariant velocity relative to the motion of the grid, which can be expressed as:

$$\boldsymbol{V_r} = \boldsymbol{V} - \boldsymbol{V_g} = (u - u_g) n_x + (v - v_g) n_y + (w - w_g) n_z \tag{3}$$

where $\boldsymbol{V_g} = u_g n_x + v_g n_y + w_g n_z$ is the contravariant velocity at the surface of the control volume. To complete the system of equations, the ideal gas equation of state is introduced: $p = \rho RT$. Additionally,

$$\Theta_x = u\tau_{xx} + v\tau_{xy} + w\tau_{xz} + k_T \frac{\partial T}{\partial x} \tag{4}$$

$$\Theta_y = u\tau_{yx} + v\tau_{yy} + w\tau_{yz} + k_T \frac{\partial T}{\partial y} \tag{5}$$

$$\Theta_z = u\tau_{zx} + v\tau_{zy} + w\tau_{zz} + k_T \frac{\partial T}{\partial z} \tag{6}$$

where k_T is the coefficient of thermal conductivity; T is the temperature. The components of the viscous stress tensor are obtained as follows:

$$\tau_{xx} = 2\mu \frac{\partial u}{\partial x} - \frac{2}{3}\mu \left(\frac{\partial u}{\partial x} + \frac{\partial v}{\partial y} + \frac{\partial w}{\partial z} \right) \tag{7}$$

$$\tau_{yy} = 2\mu \frac{\partial v}{\partial y} - \frac{2}{3}\mu \left(\frac{\partial u}{\partial x} + \frac{\partial v}{\partial y} + \frac{\partial w}{\partial z} \right) \tag{8}$$

$$\tau_{zz} = 2\mu \frac{\partial w}{\partial z} - \frac{2}{3}\mu \left(\frac{\partial u}{\partial x} + \frac{\partial v}{\partial y} + \frac{\partial w}{\partial z} \right) \tag{9}$$

$$\tau_{xy} = \tau_{yx} = \mu \left(\frac{\partial u}{\partial y} + \frac{\partial v}{\partial x} \right) \tag{10}$$

$$\tau_{xz} = \tau_{zx} = \mu \left(\frac{\partial u}{\partial z} + \frac{\partial w}{\partial x} \right) \tag{11}$$

$$\tau_{yz} = \tau_{zy} = \mu \left(\frac{\partial w}{\partial y} + \frac{\partial v}{\partial z} \right) \tag{12}$$

where μ is the viscosity coefficient.

The 6-DOF rigid body dynamic (RBD) motion is governed by.

$$m\left(\frac{dV_x}{dt} - V_y \omega_z + V_z \omega_y \right) = F_x \tag{13}$$

$$m\left(\frac{dV_y}{dt} - V_z \omega_x + V_x \omega_y \right) = F_y \tag{14}$$

$$m\left(\frac{dV_z}{dt} - V_x \omega_y + V_y \omega_x \right) = F_z \tag{15}$$

$$I_{xx} \frac{d\omega_x}{dt} - (I_{yy} - I_{zz}) \omega_y \omega_z = M_x \tag{16}$$

$$I_{yy} \frac{d\omega_y}{dt} - (I_{zz} - I_{xx}) \omega_z \omega_x = M_y \tag{17}$$

$$I_{zz} \frac{d\omega_z}{dt} - (I_{xx} - I_{yy}) \omega_x \omega_y = M_z \tag{18}$$

Eqs. (13)–(15) represent the CoG translation of the body and Eqs. (16) and (17) represents the CoG rotation in the axial system. In the above equations, m is the mass of the body, V_x, V_y, and V_z are the velocity components of the body (also the velocity of the orbiter grid, $\boldsymbol{V_g}$), ω_x, ω_y, and ω_z are the components of the angular velocity of the body, F_x, F_y, are F_z the components of applied force exerted on the body, including aerodynamic forces and gravity. In addition, I_{xx}, I_{yy}, and I_{zz} are the principal moment of inertia of the body, and M_x, M_y, and M_z are the components of the applied moment exerted on the body.

The computation of the N–S equations is based on the finite volume method [38]. The spatial discretization employs a second-order total variation diminishing (TVD) polynomials interpolation scheme with a minmod limiter [39]. The inviscid flux terms are evaluated by Harten-Lax-van Leer contact (HLLC) approximately Riemann method [40], and the viscous flux terms are calculated by the second-order simple average of all the vertex polynomials. Time advancement is performed by backward Euler integration with multi-grid acceleration and dual time step method [41]. Furthermore, the 6-DOF equations are solved by the fourth-order Runge-Kutta advancing method. The free-stream conditions are $Ma_\infty = 6.7$, $Re_\infty = 8.86 \times 10^5$ m^{-1}, $q_\infty = 24{,}217$ Pa, $p_\infty = 773$ Pa, $T_\infty = 365$ K, $p_0 = 3.95$ MPa, $T_0 = 3108$ K, and $H_0 = 3.65$ MJ kg^{-1}, which are a typical test flow conditions for the JF-12 hypersonic duplicated flight conditions shock tunnel. Due to the small Reynolds number of freestream, the flow has not transitioned to the turbulent flow with $l_b = 1$ m at such inflow condition, which has been validated by the experiments of the laminar boundary layer on a large-scale flat plate or blunt cone conducted in the JF-12 shock tunnel at similar test flow condition [42,43]. Moreover, the reliability and accuracy of the laminar flow simulation of Mach 6.7 hypersonic flows over the TSTO vehicle (i.e., Saenger concept) have been validated by Schroder et al. [44,45]. Based on the validation results, the laminar flow assumption is adopted in the simulation. The specification of fluids is the airflow with perfect gas properties. Moreover, the rarefied gas effects and non-equilibrium real gas effects [46,47] are not considered in the current study because of the relatively low total enthalpy $H_0 < 5$ MJ kg^{-1} and small Knudsen number of $1.2 \times 10^{-5} < 0.05$. Thus, the free-stream gas property is considered the calorically perfect gas, which was

also validated by Schroder et al. [44,45] through laminar flow simulations for the hypersonic flows over the TSTO vehicle. In the simulations, all conservative variables at the inflow boundary and flowfield initialization are determined by the freestream conditions. Conservative variables at the outflow boundary are computed based on the solution in the computational domain (centroidal extrapolation). Non-slip and adiabatic conditions are adopted for the wall boundary.

3.2. Computational grid and verifications

The overset grid method is used to compute the TSTO stage separation due to its advantages in simulating multibody flow problems [48]. Fig. 2 presents the computational overset grid for the TSTO vehicle and the sketch of the boundary conditions in the simulation. The overset grid comprises a booster grid as a background grid and an orbiter grid as a moving grid. Both sub-grids are generated by the hybrid meshing method and consist of structured and unstructured blocks. The first cell spacing normal to the wall is selected to ensure $y^+ \sim 1$, and a progression ratio of 1.1 is applied to cluster grid points radially outward from the wall with forty cells spanning the thickness of the boundary layer to accurately capture the boundary layer flow physics. The overset method applied in the current study involves the connection of the two sub-grids at each time step by hole cutting and data interpolation. As shown in Fig. 2, since the outer boundary of the orbiter grid serves as the cutter boundary, the booster grid cells that intersect with the cutter boundary are recognized as the cutter cells. Then, the cells are intercepted from the booster grid within the orbiter grid to form the inner boundary of the booster grid. Therefore, the cutter and inner boundary enclose the overlapping cells of the booster grid and the orbiter grid. The flow data is exchanged and interpolated on the overlapping cells to achieve second-order accuracy within two or more layers of interpolated grid nodes. Detailed overset grid methods for the numerical simulation are given in Ref. [48].

In the numerical study, three grids of different resolutions and cell numbers treated with the same meshing method are used to verify the grid independence. Three grids are labeled as the coarse, medium, and fine grid, with the total cell number of sub-grids around 8 million, 17 million, and 35 million, respectively. Fig. 3 presents the trajectory and aerodynamic coefficients of the orbiter during stage separation in the case of $l_{CoG}/l_o = 0.71$ computed from three grids. All curves of the three grids have approximately the same variation tendency, but the computational results of the medium and fine grids are more consistent at feature points. Considering the computational efficiency and cost, the medium grid is selected as the computational grid for the simulations and discussion.

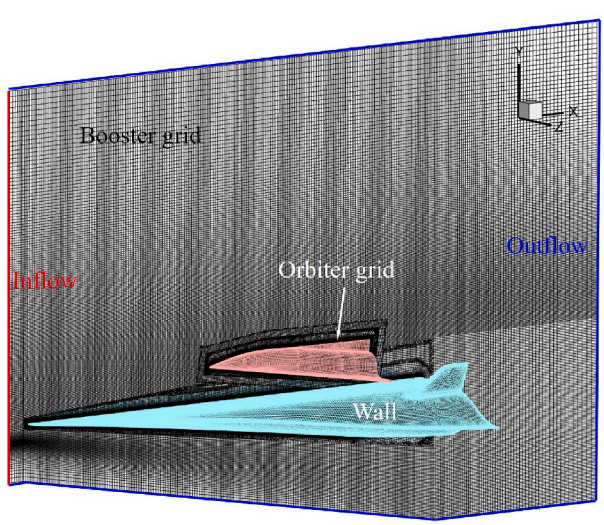

Fig. 2. Schematic of the computational overset grid for the TSTO vehicle.

To verify the computational time step independence, three different time steps with the same medium grid are used in the $l_{CoG}/l_o = 0.71$ stage separation simulation case, i.e., $dt{\cdot}U_\infty/l_b = 0.2564$, 0.1282, 0.05128, respectively. Fig. 4 shows the orbiter's displacements, pitching angle, and aerodynamic coefficients with different computational time steps. The curves for these variables have almost the same trend, but the values computed from the $dt{\cdot}U_\infty/l_b = 0.1282$ and 0.051 3 are closer. Fig. 5 shows the flowfields when the orbiter is passing by one of the separation positions with cases of different time steps. The major flow structures between these flowfields are well-captured and identical. Considering the CFD simulation accuracy and efficiency, the non-dimensional time step of $dt{\cdot}U_\infty/l_b = 0.1282$ is chosen for the simulation.

3.3. Validations

Since the hypersonic flowfield during the TSTO stage separation is mainly characterized by the SBLI phenomena and the multibody relative motion, the reliability and the efficiency of the computational methods should be validated for typical flow field cases. In this study, the shock wave-laminar boundary layer interaction and the wing-pylon-store separation cases were validated to determine the reliability and accuracy of the computational methods for simulating the TSTO hypersonic stage separation. Fig. 6 shows the experimental result and laminar flow simulation results for the laminar-SBLI at $Ma = 12.2$ and $\mathrm{Re} = 1.4 \times 10^5$ m^{-1} over the double-cone model in the LENS XX hypersonic wind tunnel [49]. The test model of a double cone has semi-angles of 25 and 55°. The pressure instrumentation was incorporated into the model to record the flowfield development over the model. In addition, the uncertainty in the experimental measurements is ±10%. The laminar flow simulation result shows good consistency with the measured data for the separation zone and feature points of the wall pressure.

Fig. 7 shows the experimental and numerical results of the supersonic wing-pylon-store separation at $Ma = 1.2$, $\mathrm{Re} = 7.87 \times 10^6$ m^{-1}. The wing-pylon-store configuration is shown in Fig. 7(a). The mass of the store is 907.8 kg, and the moments of inertia are $I_{xx} = 27.12$ kg m^2 and $I_{yy} = I_{zz} = 100$ kg m^2. More details of the geometry and experiment are depicted in Refs. [50,51]. The computational overset grid with 8.5 million cells is shown in Fig. 7(b). The computational results are obtained by solving the inviscid supersonic flow over the wing-pylon-store and 6-DOF rigid body motion equations using the overset grid method. Fig. 7(c) and (d) present the comparative results of the CFD and experiment, i.e., displacements and Euler angles of the store during separation. The computational displacements, pitching angle, and yaw angle are in good agreement with the experimental results. However, a discrepancy occurs in the roll angle when $t > 0.4$ s between CFD and the experiment. The discrepancy may be due to the smaller moment of inertia (I_{xx}) of the store in the rolling direction compared to the other moments of inertia (I_{yy} and I_{zz}), and the computational error may be amplified gradually. Overall, the comparison validates the accuracy and reliability of the computation methods for multibody separation in this study.

4. Results and discussion

4.1. Separation behavior and aerodynamics

Fig. 8 plots the linear function of the orbiter's pitching moment against the CoG before the stage separation. It can be seen that the pitching moment increases with the backward shifting of the CoG. In addition, the pitching moment equals zero at $l_{CoG}/l_o = 0.687$, which means the CoP on the orbiter is located at $l_{CoP}/l_o = 0.687$ before the release of the orbiter. On this basis, the orbiter is subjected to a pitch-up moment if the CoG is located after the CoP; otherwise, it is subjected to a pitch-down moment. When the orbiter separates from the booster, it exhibits pitch-up or pitch-down behaviors according to the positions of

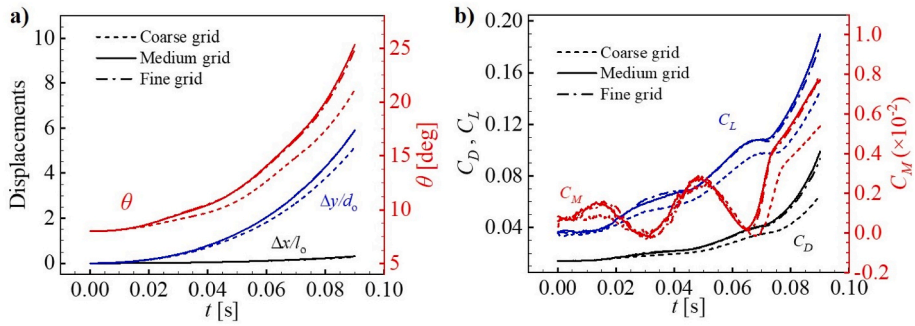

Fig. 3. Grid independency study: a) the separation displacements and pitching angle of the orbiter, and b) the aerodynamic coefficients of the orbiter during the stage separation in the case of $l_{CoG}/l_o = 0.71$ computed from three grids.

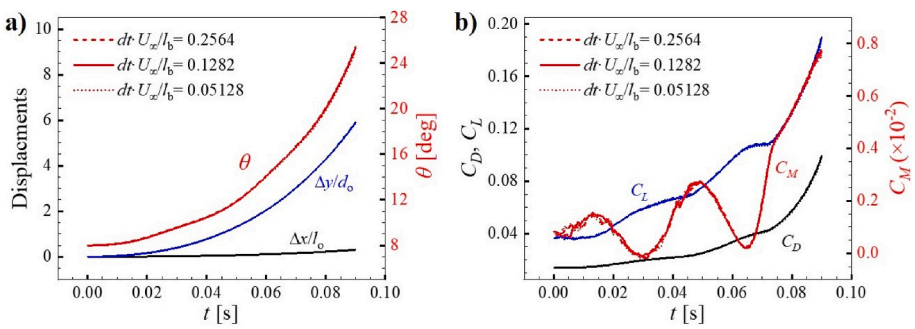

Fig. 4. Orbiter separation trajectories and aerodynamic coefficients with three different computational time steps.

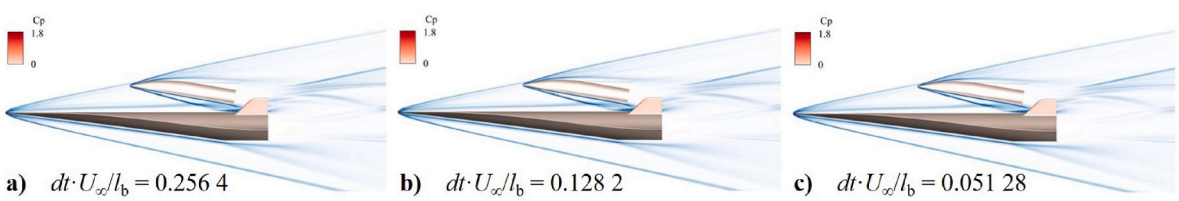

Fig. 5. Flowfields of the $t = 0.03$ s in the $l_{CoG}/l_o = 0.71$ stage separation case with three different computational time steps.

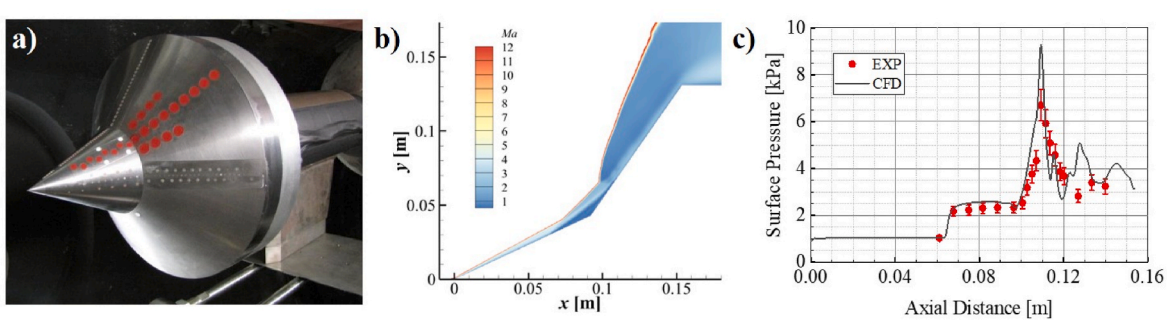

Fig. 6. Shock wave and laminar boundary layer interaction occurring on the double-cone: a) photography of double-cone test model, b) Mach number contour of the flowfield, and c) comparison of the surface pressure distribution on the double-cone between experimental and CFD results.

the CoG and CoP. Table 1 summarizes the separation results of different CoG cases: when $l_{CoG}/l_o \leq 0.687$, the orbiter collides with the booster; when $l_{CoG}/l_o = 0.70$, the orbiter falls to the booster with pitch-down behavior; when $l_{CoG}/l_o \geq 0.75$, the orbiter separates from the booster with strong interstage interaction; when $l_{CoG}/l_o = 0.80$, the orbiter experiences a somersault and causes failure; when $0.705 \leq l_{CoG}/l_o < 0.75$, the orbiter successfully separates from the booster. In addition, Fig. 9 plots the displacements and pitch angles of the orbiter for different cases. As can be seen in Fig. 9(a), when $0.65 \leq l_{CoG}/l_o \leq 0.70$ (i.e., the collision or failure cases), Δy shows a variation of first increase then decrease with the Δx. When $0.705 \leq l_{CoG}/l_o \leq 0.75$ (i.e., successful cases), Δy steadily increases with the Δx. Moreover, the slope for the successful separation cases varies from 20 to 14, and the separation displacements in all cases are tangent to and asymptotic to the line with a slope of 20 at the beginning of the separation. Therefore, the separation behaviors in these cases are the same at the beginning of the separation. Additionally, the dual lines with slopes of 20 and 14 enclose the security zone of the TSTO stage separation from the zero point. Due to

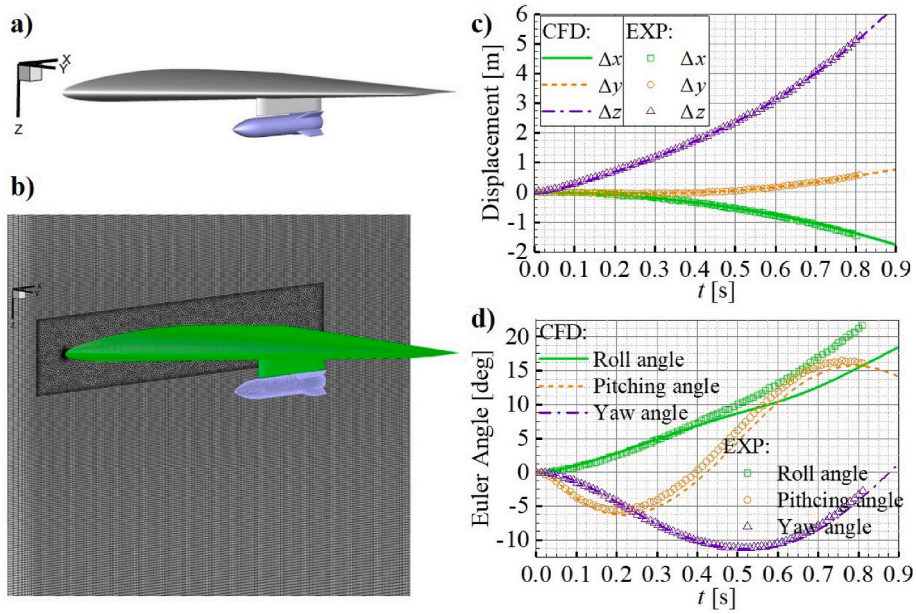

Fig. 7. Wing-pylon-store separation: a) configuration, b) computational overset grid, c) and d) are the comparisons of the displacements and Euler angles of the store during separation between experimental and computational results.

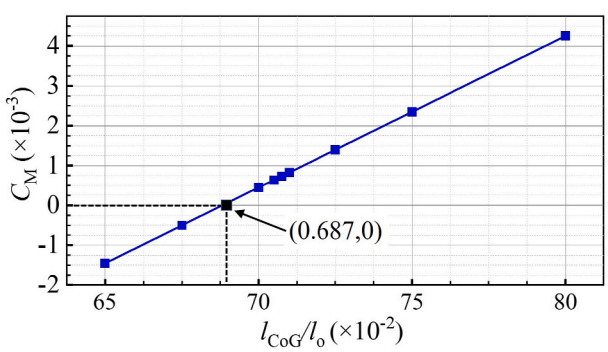

Fig. 8. The orbiter's pitching moment against the CoG before stage separation.

Table 1
Separation results of different cases.

Case	Result	Remark
l_{CoG}/l_o = 0.65	Collision	The orbiter pitches down and collides with the booster
l_{CoG}/l_o = 0.687	Collision	The orbiter pitches down and collides with the booster
l_{CoG}/l_o = 0.70	Failure	The orbiter pitches down and falls downstream
l_{CoG}/l_o = 0.705	Success	The orbiter separates away from the booster steadily
l_{CoG}/l_o = 0.725	Success	The orbiter separates away from the booster steadily
l_{CoG}/l_o = 0.75	Risk	The orbiter separates away from the booster with strong interstage interaction
l_{CoG}/l_o = 0.80	Failure	The orbiter turns a somersault with strong interstage interaction

the small security zone, the safe separation for the TSTO is challenging, and the other cases that fall outside the security boundary tend to fail. The trajectory of the orbiter presents linear variation, and the safe separation can be guaranteed at a slope between 14 and 20. As shown in Fig. 9(b), the orbiter's pitch angle eventually decreases to the negative when $0.65 \le l_{CoG}/l_o \le 0.70$, which falls into the insecurity zone. At this point, the orbiter pitches down and collides with the booster or falls into the booster's wake. When $l_{CoG}/l_o = 0.80$, the orbiter separates from the booster by somersaulting. The pitch angle of the orbiter becomes discontinuous at $+180°$ and falls into a negative value of $-180°$. It can also be seen from Fig. 9(b) that a l_{CoG}/l_o less than 0.70 may be the boundary between the pitch-up and pitch-down behavior for the stage separation.

Fig. 10 illustrates the longitudinal aerodynamic coefficients of both stages during the separation of representative cases. The C_L and C_M are calculated by Eqs. (19) and (20), respectively, where "*" is replaced by "o" and "b" for the orbiter and the booster, respectively; L denotes the lift; M_z is the pitching moment ($M_z > 0$ indicates the pitch-up moment, and $M_z < 0$ indicates the pitch-down moment). Additionally, the L also equals the normal force N since the pitch angle of the booster is fixed. During separation, the aerodynamic coefficient of the orbiter is larger than that of the booster, indicating that the orbiter suffers more from aerodynamic interference than the booster during the separation. This result agrees with the study of Wang et al. [32] In addition, the fluctuation of the aerodynamic coefficients increases with the backward shift of CoG. At $l_{CoG}/l_o = 0.75$ and 0.80, its variation trend differs from the others. When $0.65 \le l_{CoG}/l_o \le 0.70$, the lift and moment of the orbiter decrease to a negative value, resulting in the pitch-down of the orbiter and separation failure. In this CoG interval, the lift coefficient and pitch-down moment of the orbiter decrease as the CoG moves backward, and the collision moment of both stages is delayed with the CoG backward shift. During this process, the lift coefficient of the booster first decreases slightly and then increases to the undisturbed state, while the nose-up moment first increases and then decreases to the undisturbed state. The variation amplitude of the aerodynamics increases with the CoG backward shift. Regarding the successful cases ($0.70 < l_{CoG}/l_o < 0.75$), the orbiter steadily separates from the booster under positive lift and slight pitch-up moment. In this process, the lift of the orbiter increases while the pitching moment varies steadily, facilitating the rapid entry of the orbiter into orbit after stage separation. The aerodynamics coefficient of the booster follows the same trend as in the previous cases, but the variation amplitude is greater due to the larger backward shift of the CoG. After the separation, the aerodynamic coefficients of the booster converge to the undisturbed values, as shown in Fig. 10(c) and (d). The fluctuation amplitude of the aerodynamic coefficients in both stages increases with the CoG backward shift, indicating a stronger aerodynamic interaction between stages during separation. However,

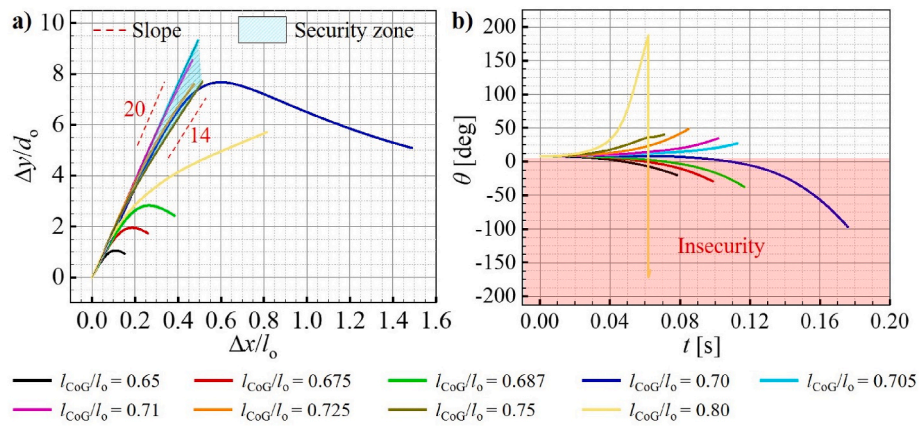

Fig. 9. The separation trajectory of the orbiter (a) and the time history of the orbiter's pitching angle (b) for different cases.

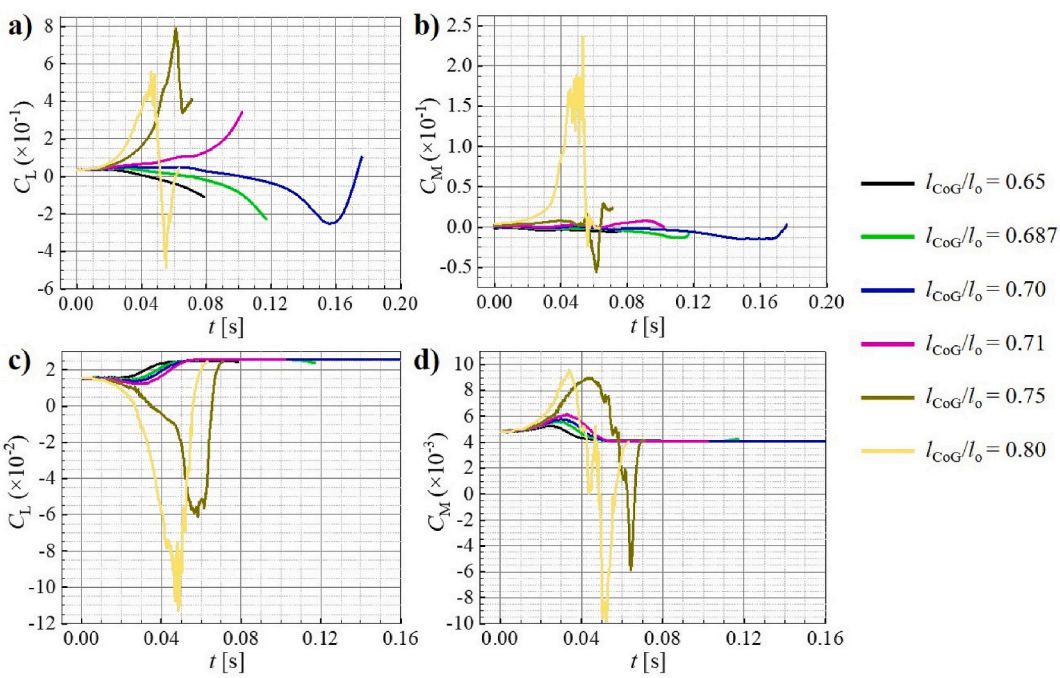

Fig. 10. Time history of the aerodynamic coefficients of the stages during separation: subfigures (a) and (b), the orbiter; subfigures (c) and (d), the booster.

the aerodynamic coefficients significantly fluctuate when $l_{CoG}/l_o = 0.75$ and 0.80, where strong and complex aerodynamic interference may happen between stages. The lift of the orbiter rises rapidly to a maximum and then drops to the minimum and finally increases. The pitching moment of the orbiter presents large fluctuation and peak characteristics during separation. In addition, the lift coefficient of the booster decreases fast to a great negative value and then quickly increases to the undisturbed value. The pitching moment of the booster increases rapidly and then decreases to the nose-down moment and finally reaches the undisturbed value. The effects of interstage aerodynamic interference on aerodynamics will be analyzed in the subsequent section with the flow patterns. Moreover, the large pitch-up moment applied to the orbiter at $l_{CoG}/l_o = 0.80$ results in the somersault of the orbiter and causes separation failure. Based on the separation behavior, the safe condition for the TSTO stage separation is $0.70 < l_{CoG}/l_o \leq 0.75$. However, given the large fluctuations in the lift and pitching moment of the stages when $l_{CoG}/l_o = 0.75$, the absolute safe condition for the TSTO stage separation is considered to be $0.70 < l_{CoG}/l_o < 0.75$.

$$C_L = \frac{L}{\frac{1}{2}\rho_\infty U_\infty^2 l_* w_*} \tag{19}$$

$$C_M = \frac{M_z}{\frac{1}{2}\rho_\infty U_\infty^2 l_*^2 w_*} \tag{20}$$

4.2. Typical flowfield patterns with aerodynamics

During stage separation, the hypersonic flow past the TSTO can be divided into three phases based on the relative position between the booster leading edge shock wave (BLES) and the orbiter: I. The orbiter is underneath the BLES; II. The BLES impinges on the orbiter when the orbiter breaks through the BLES; III. The orbiter passes through the BLES. Fig. 11 shows representative flowfield characteristics in phase I. The flowfields are presented by the numerical schlieren (contour of the density gradient) on the symmetry plane and the wall pressure coefficient contours. Additionally, the vortex iso-surface shown in the results was generated by implementing the LiutexUTA code published by Liu et al. [52,53] at the University of Texas at Arlington. Before the orbiter

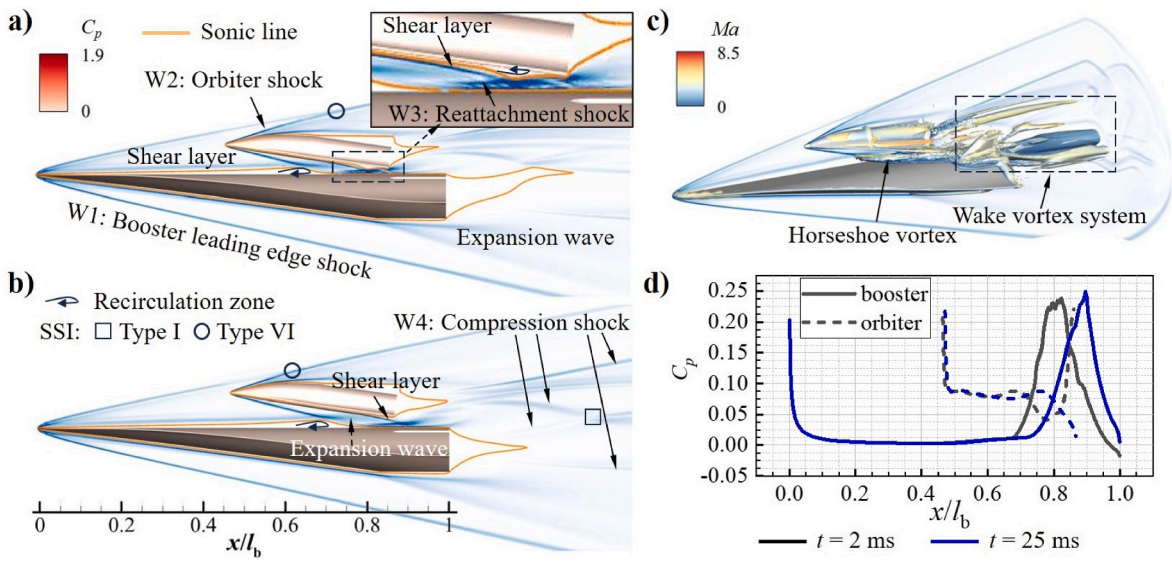

Fig. 11. The representative small interstage gap characteristic flowfields of TSTO at $l_{CoG}/l_o = 0.687$ before the orbiter passes through the BLES: (a) and (b) are the flowfields of $t = 2$ ms and 25 ms, respectively; (c) vortex structure at $t = 25$ ms shown by the iso-surface of |Liutex| = 8000 and colored with Mach number; (d) pressure coefficients along the upper wall of the booster and the lower wall of the orbiter at two instants.

passes through the BLES, the flow characteristic is dominated by the small interstage gap flow, where the orbiter shock wave W2 is reflected between the stages and induces boundary layer separation. As shown in Fig. 11(a), the SBLI occurs where the incident shock wave W2 impinges on the shear layer of the booster, which separates from the booster and forms the recirculation zone. Then, the reattachment shock wave W3 is formed as the shear layer re-attaches to the booster. However, W3 impinges on the orbiter and causes the separation of the shear layer. The impingement of the separated orbiter shear layer and the reattachment of the booster shear layer maximizes the pressure on the booster, as shown in Fig. 11(d). Therefore, the pitching moment of the booster keeps increasing, as shown in Fig. 10(d). As the stage separation proceeds and the interstage gap increases, the impinging location of W2 moves downstream, and W3 no longer impinges on the orbiter, resulting in direct impingement of the orbiter shear layer on the booster and increased pressure. As shown in Fig. 11(b), the increasing rate of the

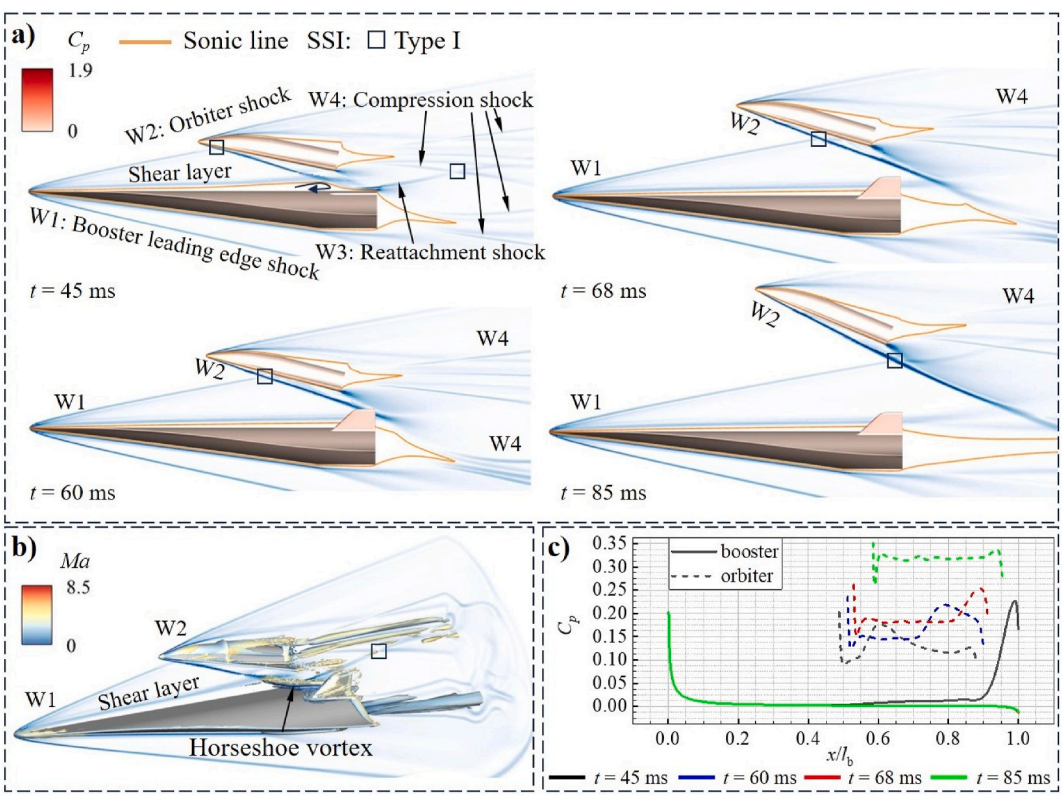

Fig. 12. The representative large interstage gap characteristics flowfields of TSTO at $l_{CoG}/l_o = 0.71$ for phase II and phase III stage separations: (a) flowfields shown by symmetry numerical schlieren and contour of wall pressure coefficient; (b) vortex structure shown by the iso-surface of the |Liutex| = 8000 and colored with the Mach number; (c) pressure coefficients along the upper wall of the booster and the lower wall of the orbiter at four instants.

pressure diminishes at $t = 25$ ms. Since the shear layer does not re-attach to the aft body at $t = 25$ ms, the pressure along the aft body decreases under the effect of the expansion wave formed by the reattachment of the booster shear layer. In addition to the complex interstage SBLI, the BLES W1 and W2 encounter type VI SSI above the orbiter, and the compression shock waves W4 encounter type I SSI in the wake flow. Fig. 11(c) also shows the typical vortex structures in phase I, including the horseshoe vortex formed by recirculation under the interstage SBLI and the wake vortex system.

Fig. 12 shows the typical flow patterns as the orbiter breaks through the BLES (W1) during stage separation. When the interstage gap becomes larger, the reflection of multiple incident shocks (orbiter shock W2) in the gap disappears and remains as a single interaction of the W2 with the booster shear layer. The reattachment shock W3 and the compression shock W4 cause type I SSI in the wake region at $t = 45$ ms, as shown in Fig. 12(a). Moreover, the incident shock W2 induces the flow separation on the booster and forms the horseshoe vortex, as shown in Fig. 12(b). As the SBLI moves downstream, the peak pressure also moves downstream and approaches the trailing edge of the booster, as shown in Fig. 12(c). It can also be seen that the transmitted shock of W2 interacts with the booster wake rather than the booster boundary layer as separation proceeds in type I SSI with the BLES. The resulting SBLI on the booster vanishes, and the booster wall pressure recovers to its undisturbed state, decreasing the pitching moment of the booster. Furthermore, the BLES first performs a type I SSI with the orbiter shock W2 and then begins to impinge on the lower wall of the orbiter from nose to tail. When 45 ms $\leq t \leq$ 68 ms, the peak pressure on the low wall of the orbiter moves from the nose downstream to the tail, as shown in Fig. 12(c). In such circumstances, the pitching moment of the orbiter first increases and then decreases. After the orbiter flies through the BLES ($t = 85$ ms), the transmitted shock wave of W1 in the type I SSI no longer impinges on the orbiter but interacts with the orbiter's wake. As a result, the wall pressure of the orbiter is restored to an undisturbed state, as shown in Fig. 12(c).

The above flowfield patterns are associated with the boundary flow separation induced by the incidence shock of W2. The incidence shock has a low intensity, leading to localized flow separation on the booster that develops downstream. However, for larger l_{CoG}/l_o (i.e., $l_{CoG}/l_o \geq 0.75$), the flowfield patterns differ significantly and involve the large flow separation and complex wave structure due to the strong incidence shock wave W2 during stage separation. Fig. 13 shows the typical flowfields for $l_{CoG}/l_o = 0.75$, and Fig. 14 plots the pressure coefficients over the wall at corresponding instants during stage separation. Since the CoG is located near the rear of the orbiter, the pitching moment and pitching angle of the orbiter are larger, as shown in Fig. 9(b) and 10(b). It can be seen from Fig. 13(a) that the stronger incident orbiter shock W2 with a larger shock angle leads to a larger flow separation on the booster. The separated shear layer W3 induces the impingement of the separation shock W4 on the orbiter, increasing the pressures on the lower wall of the orbiter and the pitching moment, as shown in Fig. 14(b). In turn, the increasing strength of W2 causes stronger SBLI on the booster, leading to the impingement of the separated shear layer on the orbiter and greater

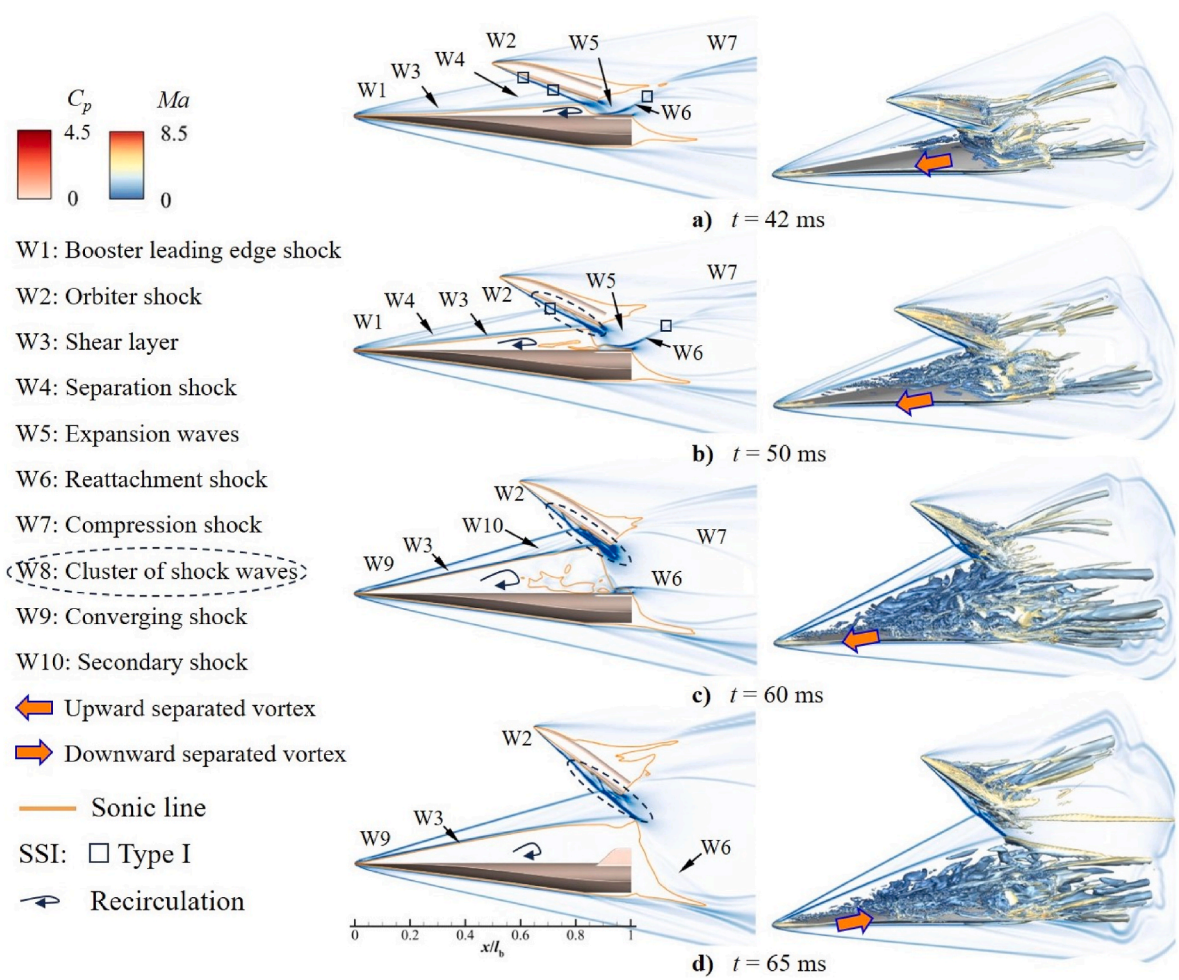

Fig. 13. The complex flowfield patterns with larger interstage gap characteristics over TSTO of several instants during stage separation at $l_{CoG}/l_o = 0.75$ (left, numerical schlieren on the symmetry plane and wall pressure coefficient contours; right, vortex structure shown by iso-surface of the |Liutex| = 8000 and colored with the Mach number).

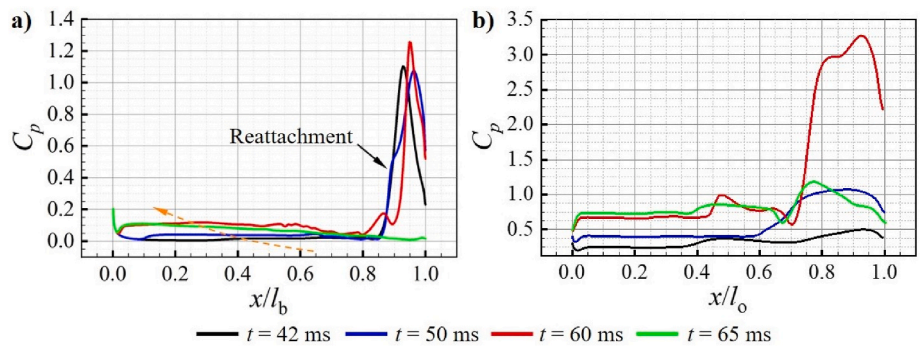

Fig. 14. Pressure coefficients over the upper wall of the booster (a) and the lower wall of the orbiter (b) of several instants during stage separation at $l_{CoG}/l_o = 0.75$.

pressures, as shown in Fig. 13(b) and 14(b). Under the effects of the shear layer reattachment and the expansion waves behind the orbiter, the formed reattachment shock W6 is strong and impinges on the booster nearly as a bow shock wave, inducing great pressure on the booster, as shown in Fig. 14(a). Therefore, a strong adverse pressure gradient is formed and propagates upstream through the subsonic recirculation zone underneath the shear layer. The boundary layer on the booster rapidly separates and turns into a large-scale separated vortex moving upstream, as shown in Fig. 13(a)-13(c). In this process, the induced separation shock W4 moves upstream with the lifting shear layer and causes type I SSI with the W1 and W2. The transmitted shock waves of W1 and W4 are reflected in the limitation of the W2 and the orbiter wall, forming the shock wave cluster shown in Fig. 13(b) and inducing pressure fluctuations in the lower wall of the orbiter shown in Fig. 14(b). With the further destabilization of the booster boundary layer flow and upstream movement of the separating vortex, W4 and W1 converge into the stronger converging shock W9. Together with the fully separated shear layer, the W9 impinges on the orbiter, creating a more complex cluster of shock waves at the lower wall of the orbiter with greater pressures, as shown in Fig. 13(c) and 14(b). The reattachment shock W6 becomes stronger and swings downstream due to the fully separated flow and the high-speed jet flow accompanying the accelerated expansion wave behind the orbiter. It interacts with the booster's wake rather than the orbiter's wake to adapt the supersonic flow downstream of the larger recirculation zone. The pressure on the booster around the reattachment shock position increases, and the pressure along the recirculation zone reaches its maximum due to the strongest compression effect of the W9, as shown in Fig. 14(b). Additionally, the fully separated shear layer folds, and some small secondary shock waves are formed due to the irregular motion of the large-scale separated vortex, as shown in Fig. 13(c). As the separation proceeds, the orbiter flies to the position where the strong downstream blocking condition formed by the interaction of the W2 and W9 with the separated flow has vanished, and the shear layer W3 no longer impinges on the orbiter but gradually re-attaches to the booster. The reattachment shock W6 no longer presents on the booster, eliminating both the pressure peak and adverse pressure gradient, as shown in Fig. 14(b). As a result, the separated vortex loses its support conditions and moves downstream to the wake flow, as shown in Fig. 13(d).

Fig. 15 shows strong aerodynamic interactions during the stage separation when the CoG is further shifted backward (i.e., $l_{CoG}/l_o = 0.80$). When $l_{CoG}/l_o = 0.80$, the flowfield patterns before $t = 50$ ms are similar to those at $l_{CoG}/l_o = 0.75$, as shown in Fig. 13. However, a larger pitching moment leads to a larger incidence angle and stronger

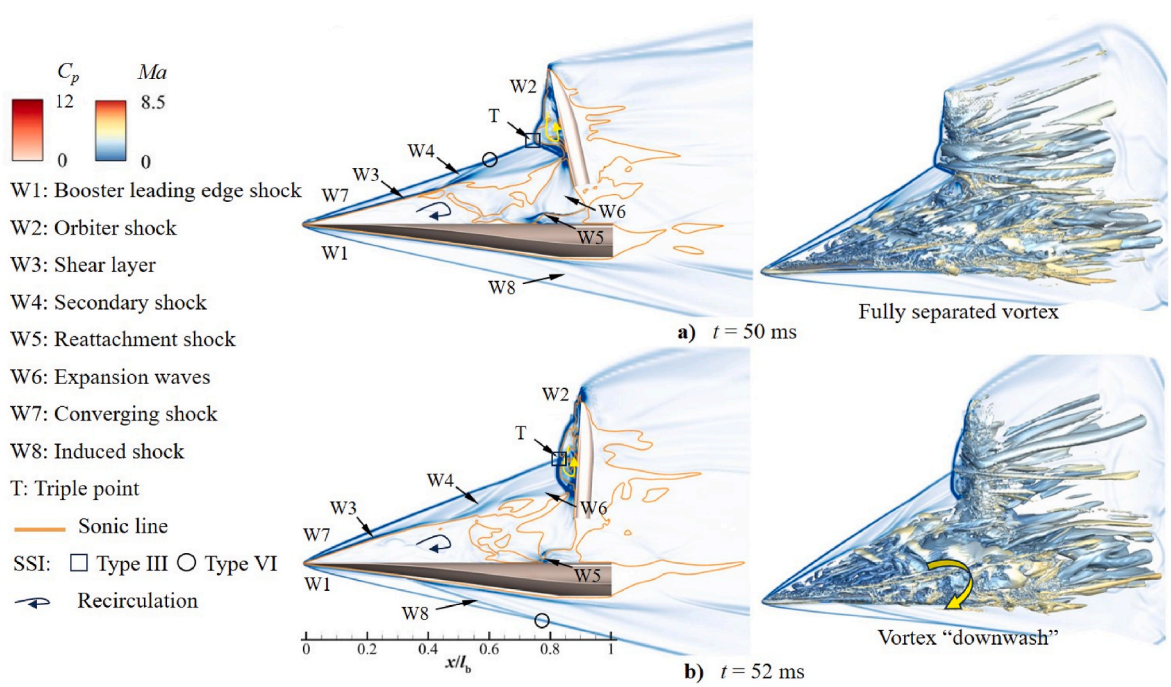

Fig. 15. Strong aerodynamic interaction causing longitudinal rolling of the orbiter in the case of $l_{CoG}/l_o = 0.80$. (left, numerical schlieren on the symmetry plane and wall pressure contour; right, vortex structure shown by iso-surface of |Liutex| = 8000 and colored by Mach number).

downstream conditions between the orbiter and the booster, enhancing the recirculation motion underneath the shear layer, as shown in Fig. 15. The larger and stronger recirculation region forms a stronger shear layer W3 and converging shock W8. The folding shear layer caused by the vortex results in type VI SSI interaction between the secondary shock W4 and W7. Then, the strong W7 interacts with the orbiter shock W2 with type III SSI and forms the triple point. The strong interaction leads to flow separation in the lower wall of the orbiter and the formation of the corresponding separated vortex system. As shown in Fig. 15(b), the third shock wave in the type III SSI will generate a large pressure as it impinges on the orbiter and increases the pitching moment, causing longitudinal rolling of the orbiter. Due to the full separation of the booster, the BLES (W1) will be detached from the leading edge, and the booster will suffer a significant loss of "wave-ride" performance. As a result, the pressure on the lower wall along the leading edge no longer exceeds the pressure along the upper wall. The strong vortex is downwardly directed along the leading edge, propagating from the downstream to upstream during the longitudinal rolling of the orbiter due to the increasing strength of the separated vortex. Fig. 15 shows that the vortex downwash behavior induces shock W8 along the shear layer on the lower wall of the booster, which moves from the downstream to upstream with increasing strength. The strong interaction pattern continues until the end of the longitudinal rolling of the orbiter and the disappearance of the strong downstream obstruction conditions. Furthermore, due to the increased compression effect of the converging shock W7 and the upstream shifting of the reattachment shock W5, as well as the loss of the wave-ride performance of the booster, the pitching moment reaches its minimum around $t = 50$ ms, as shown in Fig. 10(d).

4.3. Analysis of longitudinal dynamic stability

Since the TSTO vehicle has a symmetric configuration, the rolling and yaw motions are insignificant during stage separation. Therefore, the longitudinal dynamic stability concerned with the pitching motion is analyzed in depth from several aspects. The conventional analysis method for the dynamic stability of the aeronautical vehicle is based on two simplifying assumptions: small disturbance with small variation in the variable; and linear changes in aerodynamics with motion variables [54]. However, these assumptions may no longer be valid because SSI, SBLI, and flow separation produce stronger aerodynamic disturbances during hypersonic stage separation of TSTO vehicles. Thus, an alternative and candidate analysis method based on the CoP characteristics for the longitudinal dynamic stability is proposed and applied in TSTO stage separation.

4.3.1. CoP peak characteristics

The CoP is defined as the point on the body where the aerodynamic moment is zero. It is located at a distance x_{CoP} downstream of the leading edge of the vehicle [55]:

$$x_{\mathrm{CoP}} = l_{\mathrm{CoG}} - \frac{M_z}{N} \tag{21}$$

the non-dimensional distance between the CoP and CoG is considered as the CoP characteristic to reflect the longitudinal dynamic stability:

$$\left(\frac{x_{\mathrm{CoP}} - l_{\mathrm{CoG}}}{l}\right)_* = -\left(\frac{M_z}{N \cdot l}\right)_* . \tag{22}$$

where N is the normal force; l is the vehicle length; the symbol "*" is replaced by the "o" and "b" for the orbiter and the booster, respectively. As for Eq. (21), the pitching moment results in a pitch-up or pitch-down trend when the CoP is upstream of the CoG or downstream of the CoG. Because the pitching moment affects the separating stability, the time history of the CoP is important. Fig. 16 shows the CoP characteristics of the orbiter and the booster in different stage separation cases. As shown in Fig. 16(a), at $0.65 \le l_{\mathrm{CoG}}/l_{\mathrm{o}} \le 0.70$, the CoPs of the orbiter significantly change, presenting drastic "peak" characteristics. Because the normal force of the orbiter changes from the positive to the negative, the CoP first increases to a greater positive value and then drops to a greater negative value, while the pitching moment changes steadily during this time. The drastic "peak" characteristic of the CoP indicates an unsafe separation mode due to the sharp changes in the longitudinal dynamic aerodynamic characteristics over a very short period. This finding can also be validated by the separation results at $0.65 \le l_{\mathrm{CoG}}/l_{\mathrm{o}} \le 0.70$, as shown in Table 1. It can also be seen from Fig. 9 that the above finding is consistent with the result and analysis of the orbiter's motion. Expect for the separation cases at $0.65 \le l_{\mathrm{CoG}}/l_{\mathrm{o}} \le 0.70$, the CoP characteristics of

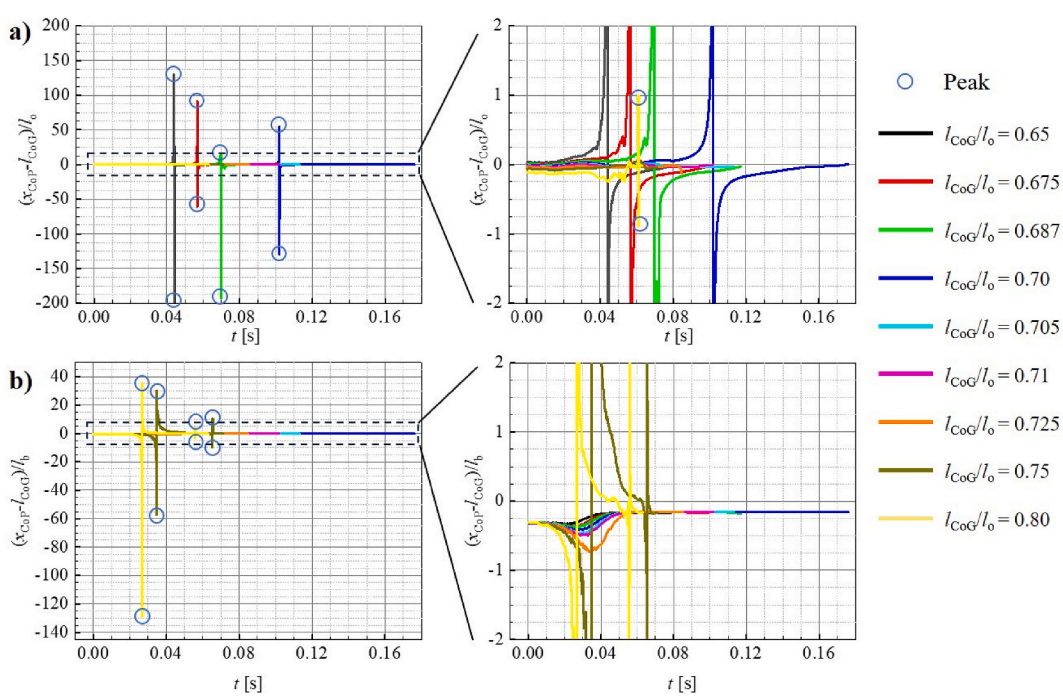

Fig. 16. Time history of the CoP for the orbiter (a) and the booster (b) in the different stage separation cases.

the remaining cases are also displayed in the enlarged plots of Fig. 16(a). In contrast to the drastic "peak" characteristics, the time history of the CoP in these cases shows a relatively stable pattern and evolves approximately along the zero axis, except for the case of $l_{CoG}/l_o = 0.80$. This result suggests that the CoP is close to the CoG, with a stable and safe separation of the orbiter from the booster throughout the separation process. Fig. 15 shows that when $l_{CoG}/l_o = 0.80$, the orbiter experiences strong aerodynamic interference, and the flow separation on the fuselage is large. Accordingly, the aerodynamics exerted on the orbiter fluctuates, and the dynamic characteristic of the CoP eventually oscillates and diverges. This characteristic also shows the unsafe separation mode, which can be validated in the previous discussion for Fig. 15. Thus, the separation cases of $0.65 \le l_{CoG}/l_o \le 0.70$ and $l_{CoG}/l_o = 0.80$ are unsafe according to the CoP characteristics of the orbiter and are also unexpected in the stage separation of TSTO.

The "peak" characteristics also appear in the time history of the booster CoP for the cases of $l_{CoG}/l_o = 0.75$ and 0.80, with two pairs of "peaks" observed, as shown in Fig. 16(b). In each pair of "peaks", the COP of the booster changes in the same way by dropping to a negative value and then rising sharply to a positive value. However, the variations of the first and the second pair of "peaks" are due to different factors. Taking the case of $l_{CoG}/l_o = 0.75$ as an example, in the first pair of peaks around $t = 35$ ms, the normal force of the booster decreases from the positive to zero and negative values. The booster is subjected to a strong reattachment shock impingement on the upper wall, resulting in pressure rise when the pitch-up moment is applied, as shown in Fig. 13 (a). In the second pair of peaks around $t = 65$ ms, the normal force of the booster increases from negative to zero and positive values. Because of the strong reattachment, the shock wave disappears, and the converging shock weakens (Fig. 13(d)), the pressure distribution on the upper surface of the booster decreases (Fig. 14(a)), and the pitching moment changes from the pitch-down to pitch-up (Fig. 10(d)). The CoP characteristics in the case of $l_{CoG}/l_o = 0.80$ are similar to those at $l_{CoG}/l_o = 0.75$ because their aerodynamic interference processes and mechanisms are similar to those discussed in the previous section. Moreover, the separation process may also be unsafe and unexpected for the cases of $l_{CoG}/l_o = 0.75$ and 0.80. The "peak" characteristics of the booster CoP are detrimental to the flight stability of the booster during TSTO stage separation. Overall, by analyzing the CoP characteristics of the two stages, the safer separation condition for the TSTO model at zero angle of attack is $0.70 < l_{CoG}/l_o < 0.75$, which agrees well with the safe separation condition inferred from the aerodynamics in Sec. 4.1. Moreover, in the case of dynamic CoP under strong disturbance, if the "peak" characteristic is observed, the longitudinal dynamic stability performance is poor, and the stage separation is not probably safe; otherwise, the stage separation might be safe.

4.3.2. Derivative of CoP to time

When the "peak" characteristic is observed in the CoP time history of a given stage, this stage experiences longitudinal dynamic instability, leading to stage separation failure. Thus, the CoP dynamic behavior should be monitored to predict the possibility of the "peak" characteristic and provide instruction for separation safety. The derivative of the CoP to the time can be used as a second observational view of the longitudinal dynamic stability to provide alternative safe separation judgments. Fig. 17 illustrates the non-dimensional derivation of the CoP to time for both stages between different stage separation cases. For the unstable separation cases with "peak" characteristics, the derivative of the CoP to time first oscillates around the zero point and gradually diverges with rapid rise and drops. Conversely, the longitudinal dynamics in these cases are stable without "peak" characteristics, which is manifested by a small oscillation amplitude around the zero value of the first derivative CoP with time throughout the stage separation. If the derivative of CoP to time is considered as an alternative index for the longitudinal dynamic stability under the complex and strong disturbance circumstance, and comparing the derivative of CoP to time for two groups of separation cases (i.e., stable and unstable cases), the safety thresholds in terms of the longitudinal dynamic stability for the orbiter can be expressed as:

$$\left|\frac{\partial(x_{CoP} - l_{CoG})_o / l_o}{\partial t} \cdot \frac{l_o}{U_\infty}\right| \le 0.02 \tag{23}$$

and that for the booster can be expressed as:

$$\left|\frac{\partial(x_{CoP} - l_{CoG})_b / l_b}{\partial t} \cdot \frac{l_b}{U_\infty}\right| \le 0.2 \tag{24}$$

From the dynamic characteristics of the CoP, the above thresholds can also determine the safe condition for the TSTO stage separation. For example, in the cases of $0.70 < l_{CoG}/l_o < 0.75$, their first derivates of CoP to time vary and oscillate within the threshold during the stage separation. The aerodynamics on both stages caused by the aerodynamic interference become consistent and smooth, and the longitudinal dynamics are more stabilized. For the cases of $l_{CoG}/l_o \le 0.70$ and $l_{CoG}/l_o \ge 0.75$, their first derivates of CoP to time oscillate with the divergence tendency. Then, the "peak" characteristics occur after a sudden loss of control due to the reversal of the normal force induced by the strong and complex interference. Moreover, the flow separation on the stage also contributes to the oscillation of the longitudinal dynamic stability, with stronger and larger flow separation producing greater oscillations, such as the fully separated flow on the booster at $l_{CoG}/l_o = 0.75$ and 0.80 (Figs. 13 and 15). The drastic fluctuation and oscillation of the derivate of CoP to time are shown in Fig. 17(b), with large-scale fully separated vortex responsible for the longitudinal aerodynamic instability.

4.3.3. Linear stability analysis

Although the associated assumptions and limited conditions may not be appropriate, the traditional linear stability analysis of the TSTO stage

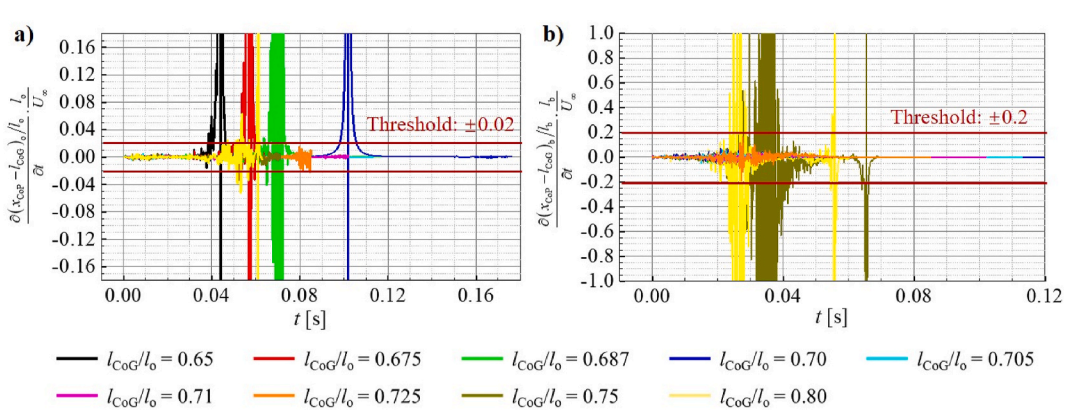

Fig. 17. Time history of the first derivative of CoP to time for the orbiter (a) and the booster (b) in different stage separation cases.

separation is still performed to show the prediction behavior of the linear stability theory. The traditional longitudinal stability criterion for the re-entry vehicle is based on simplified assumptions, which can be expressed as [56]:

$$C_{Mq^*} + C_{M\dot{\alpha}^*} < 0 \tag{25}$$

where C_{Mq^*} is the first derivate of C_M to the non-dimensional pitch angle rate q^*; $C_{M\dot{\alpha}^*}$ is the first derivate of C_M to the non-dimensional rate of the angle of attack. Eq. (25) indicates that the pitch attenuation parameter is a separate measure of dynamic stability. When it is negative, the vehicle is probably stable because the pitching moment attenuates forward, and the CoP dynamically reaches the CoG during the flight. Fig. 18 plots the pitch attenuation parameter for the orbiter in the different stage separation cases. Considering that the angle of attack and the pitching angle for the orbiter are the same during separation, their rates are equal, and their non-dimensional forms can be expressed as follows:

$$\dot{\alpha}^* = \frac{\dot{\alpha} l_o}{2U_\infty}, q^* = \frac{q l_o}{2U_\infty} \tag{26}$$

Since the booster is fixed during the simulations of stage separation, the pitch attenuation parameter is absent and cannot be discussed here. As shown in Fig. 18, the pitch attenuation parameter has the "peak" characteristics in some cases regardless of whether the stage separation is safe or unsafe, even in the case of failed separation at $l_{CoG}/l_o = 0.65$ and 0.675. In addition, the pitch attenuation parameters between these cases (stable or unstable stage separation) fluctuate in a range above or below zero with several "peaks" rather than exhibiting a negative or non-negative characterization. Therefore, in the TSTO stage separation situation with complex and strong aerodynamic interference, the pitch attenuation parameter loses its characterization effect on the longitudinal dynamic stability, as expressed by Eq. (25). This phenomenon further supports the desirability of alternative characterization metrics for the longitudinal dynamic stability involved in CoP dynamic properties in the case of TSTO stage separation. Table 2 summarizes three analysis methods proposed and discussed in the longitudinal dynamic stability study of TSTO stage separation.

5. Conclusions

This study investigates the effects of the CoG on the stage separation of TSTO vehicles at Mach 6.7. New insights into the dynamic characteristics of the TSTO stage separation and safe separation criteria are obtained. Furthermore, the dynamic separation behavior, unsteady aerodynamic interaction mechanism with flowfield patterns, and the longitudinal dynamic stability based on the CoP are analyzed for the cases at $0.65 \le l_{CoG}/l_o \le 0.80$. The conclusions of this study are as follows:

(1) The CoG of the orbiter contributes to the stage separation of TSTO, with a safe separation condition of $0.70 < l_{CoG}/l_o < 0.75$. For the separation behavior, the trajectory of the orbiter presents linear variation, and the safe separation can be guaranteed at a slope between 14 and 20. The small size of the security zone makes it challenging for TSTO to be safely separated. When $l_{CoG}/l_o \le 0.70$, the orbiter pitches down and collides with the booster, leading to separation failure. In the cases of $l_{CoG}/l_o \ge 0.75$, strong aerodynamic interference and large flow separation occur in both stages, resulting in the somersault of the orbiter and the risk of the stage separation. Under the strong aerodynamic interference, the peak value of the stages' aerodynamics at $l_{CoG}/l_o \ge 0.75$ is at least about four times larger than that at $l_{CoG}/l_o < 0.75$. Moreover, the pitching angle of the orbiter when $l_{CoG}/l_o = 0.80$ is at least about three times greater than that for the other cases.

(2) The hypersonic flowfield patterns past TSTO can be divided into three phases based on the relative position between the BLES and the orbiter. When the orbiter is below the BLES, the multiple SBLI between stages changes to the single SBLI as the interstage gap increases. The interstage SBLI causes the horseshoe vortex and pressure-rising. The pressure increase at the reattachment position is approximately 20 times the plateau pressure at the recirculation region on the upper wall of the booster. As the orbiter breaks through the BLES, the interaction between the BLES and the orbiter affects the aerodynamics of the orbiter. Due to the

Table 2
Analysis methods and criteria of the longitudinal dynamic stability in stage separation.

No.	Method	Criteria
1	CoP characteristics	Stable and safe: No "peak" characteristics appear for both stages
2	Derivative of CoP to time	Stable and safe: $\left\lvert \frac{\partial(x_{CoP} - l_{CoG})_o/l_o}{\partial t} \cdot \frac{l_o}{U_\infty} \right\rvert \le 0.02$ and $\left\lvert \frac{\partial(x_{CoP} - l_{CoG})_b/l_b}{\partial t} \cdot \frac{l_b}{U_\infty} \right\rvert \le 0.2$
3	Traditional linear dynamic stability analysis	$C_{Mq^*} + C_{M\dot{\alpha}^*} < 0$ loses efficacy for the TSTO stage separation situation

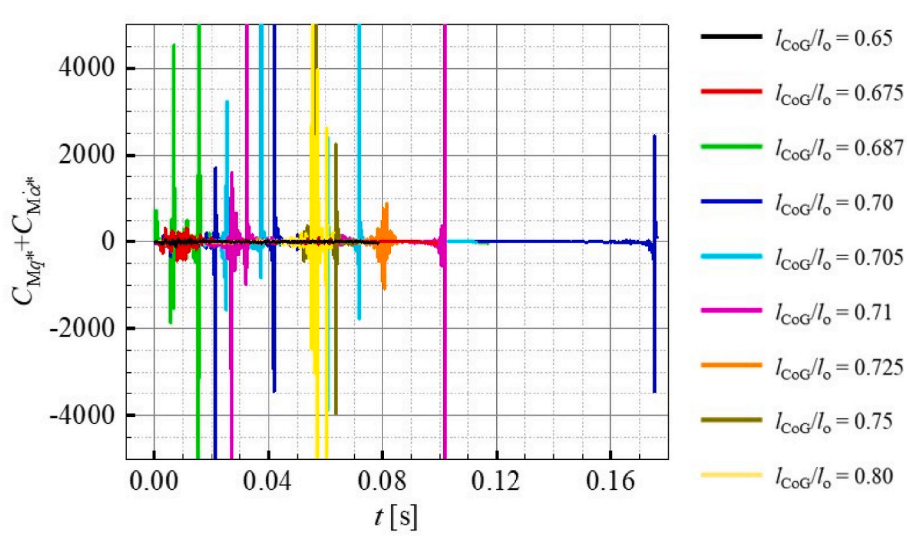

Fig. 18. Time history of the orbiter's pitch attenuation parameter in different stage separation cases.

modest strength of the BLES, the pressure rise at the shock-impinging position is approximately twice the plateau pressure on the lower wall of the orbiter. Once the orbiter passes through the BLES without strong SSI, the separation is secured. Moreover, the mechanism of unsteady interaction between the shifting of SBLI and the aerodynamics is revealed. Particularly, the risk of stage separation due to strong aerodynamic interference involved with the large flow separation and strong shock structure is analyzed in detail for the cases of $l_{CoG}/l_o = 0.75$ and 0.80. Under the strong aerodynamic interference when $l_{CoG}/l_o = 0.75$, the pressure at the position of the reattachment shock wave is at least 24 times higher than the plateau pressure in the recirculation region on the upper wall of the booster. In addition, the pressure rises at least four times the plateau pressure on the lower wall of the orbiter.

(3) Based on the dynamic CoP characteristics and derivative of CoP to time, the longitudinal dynamic stability analysis is performed for the TSTO stage separation situation with complex and strong disturbance. First, the CoP characteristic representing the stable and safe separation condition is the absence of "peak" characteristics in both stages. Second, the non-dimensional derivative of CoP to time representing the stable and safe separation condition is the variation and oscillation of the derivative around the zero, with critical values of ±0.02 and ± 0.2 for the orbiter and the booster, respectively. Moreover, the mechanism of "peak" characteristics and the oscillation of the derivative with the aerodynamic interference are revealed. In addition, the traditional linear stability analysis method and criteria are demonstrated to be inefficient in accessing dynamic stability under strong and complex aerodynamic interference.

These findings provide new insights into the dynamic stability of CoP. The alternative analysis methods of longitudinal dynamic stability are clarified and will be further applied, studied, and improved in future studies. Effects such as angle of attack and staging Mach numbers will be considered in the aerodynamics of TSTO stage separation or strong disturbance instability in other vehicles.

Declaration of competing interest

The authors declare that they have no known competing financial interests or personal relationships that could have appeared to influence the work reported in this paper.

Acknowledgments

This study was co-supported by the National Natural Science Foundation of China (Nos. 11672357 and 11727901).

Nomenclature

C_D	Drag coefficient
C_L	Lift coefficient
C_M	Pitching moment coefficient
C_{Mq^*}	First derivate of C_M to the non-dimensional pitch angle rate
$C_{M\dot{\alpha}^*}$	First derivate of C_M to the non-dimensional rate of the angle of attack
C_p	Pressure coefficient
D	Drag force (N)
d	Height of vehicle (m)
dt	Dimensional time step (s)
E, H	Total energy and total enthalpy per unit mass (J·kg^{-1})
$\boldsymbol{F_c}$	Convective fluxes
$\boldsymbol{F_v}$	Viscous fluxes
F_x, F_y, F_z	Force components exerted on the body (N)
h	Height of center of gravity or interstage gap (m)
I_{xx}	Moment of inertia about the X axis (kg·m^2)
I_{yy}	Moment of inertia about the Y axis (kg·m^2)
I_{zz}	Moment of inertia about the Z axis (kg·m^2)
k_T	Coefficient of thermal conductivity (W·(m·K)$^{-1}$)
L	Lift force (N)
l	Length (m)
Ma	Mach number
M_x, M_y, M_z	Moment components exerted on body (N·m)
m	Mass (kg)
N	Normal force (N)
p	Pressure (Pa)
q	Dynamic pressure (Pa)
q^*	Dimensional pitch angle rate (rad·s^{-1})
Re	Unit Reynolds number (m^{-1})
T	Temperature (K)
t	Time (s)
U	Speed (m·s^{-1})
u, v, w	Velocity components in x, y, and z directions (m·s^{-1})
$\boldsymbol{V_g}$	Contravariant velocity vector at the surface of the control volume (m·s^{-1})
$\boldsymbol{V_r}$	Contravariant velocity vector relative to the motion of the grid (m·s^{-1})
V_x, V_y, V_z	Velocity components of body (m·s^{-1})
$\boldsymbol{W}$	Vectors of conservative variables
w	Span of vehicle (m)

x	Coordinate in the X direction (m)
y^+	Non-dimensional wall spacing
$\dot{\alpha}$	Dimensional rate of the angle of attack (rad·s^{-1})
Δx, Δy, Δz	Displacement in the X, Y, *and* Z direction (m)
$\boldsymbol{\Theta}$	Heat conduction (W·m^{-2})
θ	Pitching angle (deg)
μ	Coefficient of viscosity (N·s·m^{-2})
ρ	Density (kg·m^{-3})
$\tau_{i,j}$	Component of viscous stress (N·m^{-2})
ω_x, ω_y, ω_z	Angular velocity components of body (rad·s^{-1})

Subscripts

b	Booster
CoG	Center of gravity
CoP	Center of pressure
o	Orbiter
0	Total condition
∞	Freestream condition

References

[1] S. Weingertner, SAENGER - the reference concept of the German hypersonics technology program, in: 5th International Aerospace Planes and Hypersonics Technologies Conference, AIAA Paper No. AIAA-93-5161, 1993.

[2] F. Deneu, M. Malassigne, O. Le-couls, P. Baiocco, Promising solutions for fully reusable two-stage-to-orbit configurations, Acta Astronaut. 56 (2005) 729–736.

[3] L. McKinney, D. Farrell, T. Bogar, J. Stemler, Investigation of TSTO propulsion system options, in: 14th AIAA/AHI Space Planes and Hypersonic Systems and Technologies Conference, AIAA Paper No. AIAA-2006-8054, 2006.

[4] Y.P. Wang, H. Ozawa, H. Koyama, Y. Nakamura, Abort separation of launch escape system using aerodynamic interference, AIAA J. 51 (2012) 270–275.

[5] L.L. Jiang, H. Jia, X. Xu, W. Rong, W. Jiang, Q. Wang, G. Chen, X.P. Xue, Numerical study on aerodynamic performance of Mars parachute models with geometric porosities, Space: Sci. Technol. (2022) 9851982.

[6] S.J. Laurence, N.J. Parziale, R. Deiterding, Dynamical separation of spherical bodies in supersonic flow, J. Fluid Mech. 713 (2012) 159–182.

[7] V. Cardona, V. Lago, Aerodynamic forces of interacting spheres representative of space debris re-entry: experiments in a supersonic rarefied wind-tunnel, Acta Astronaut. 191 (2022) 148–159.

[8] S.H. Park, J. Kim, I. Choi, G. Park, Experimental study of separation behavior of two bodies in hypersonic flow, Acta Astronaut. 181 (2021) 414–426.

[9] D. Peng, F.T. Xie, X. Liu, J.Z. Lin, Y.Z. Li, J. Zhong, Q.H. Zhang, Y.Z. Liu, Experimental study on hypersonic shock–body interaction between bodies in close proximity using translucent fast pressure- and temperature-sensitive paints, Exp. Fluid 61 (2020) 120.

[10] P. Liao, W. Song, P. Du, F. Feng, Aerodynamic interference reduction using aerospike for two-stage reusable launch vehicle, J. Aero. Eng. 36 (2023) 06023002.

[11] J.H. Jia, D.B. Fu, Z.P. He, J.F. Yang, L.J. Hu, Hypersonic aerodynamic interference investigation for a two-stage-to-orbit model, Acta Astronaut. 168 (2020) 138–145.

[12] J.M. Cheng, R.Q. Chen, R.F. Qiu, W.Q. Sun, Y.C. You, Aerothermodynamic study of Two-Stage-To-Orbit system composed of wide-speed-range vehicle and rocket, Acta Astronaut. 183 (2021) 330–345.

[13] Y. Wang, Y.P. Wang, Z.L. Jiang, Unsteady interaction mechanism of transverse stage separation in hypersonic flow for a two-stage-to-orbit vehicle, Phys. Fluids 35 (2023) 056120.

[14] G.X. Xiang, C. Wang, H.H. Teng, Z.L. Jiang, Shock/shock interactions between bodies and wings, Chin. J. Aeronaut. 31 (2018) 255–261.

[15] A. Anazadehsayed, M. Barzegar Gerdroodbary, Y. Amini, R. Moradi, Mixing augmentation of transverse hydrogen jet by injection of micro air jets in supersonic crossflow, Acta Astronaut. 137 (2017) 403–414.

[16] M. Barzegar Gerdroodbary, D.D. Ganji, Y. Amini, Numerical study of shock wave interaction on transverse jets through multiport injector arrays in supersonic crossflow, Acta Astronaut. 115 (2015) 422–433.

[17] M. Barzegar Gerdroodbary, Younes Amini, D.D. Ganji, M. Rahimi Takam, The flow feature of transverse hydrogen jet in presence of micro air jets in supersonic flow, Adv. Space Res. 59 (2017) 1330–1340.

[18] Rasoul Moradi, A. Mahyari, M. Barzegar Gerdroodbary, A. Abdollahi, Younes Amini, Shape effect of cavity flameholder on mixing zone of hydrogen jet at supersonic flow, Int. J. Hydrogen Energy 43 (2018) 16364–16372.

[19] Amirhossein Edalatpour, A. Hassanvand, M. Barzegar Gerdroodbary, Rasoul Moradi, Y. Amini, Injection of multi hydrogen jets within cavity flameholder at supersonic flow, Int. J. Hydrogen Energy 44 (2019) 13923–13931.

[20] Y. Wang, Y.P. Wang, Z.L. Jiang, Numerical investigation of aerodynamic separation schemes for two-stage-to-orbit-like two-body system, Aero. Sci. Technol. 131 (2022) 107995.

[21] Y. Wang, Y.P. Wang, C. Wang, Z.L. Jiang, Numerical study of longitudinal stage separation for parallel-staged two-stage-to-orbit vehicle, Acta Aeronautica Astronautica Sinica 44 (2023) 127634 (in Chinese).

[22] Y. Wang, Y.P. Wang, C. Wang, Z.L. Jiang, Numerical investigation on longitudinal stage separation of spiked Two-Stage-to-Orbit vehicle, J. Spacecraft Rockets 60 (2023) 215–229.

[23] Y. Wang, Y.P. Wang, Z.L. Jiang, Experimental study of longitudinal stage separation of two-body configuration in shock tunnel, AIAA J. 60 (2022) 6940–6946.

[24] Y. Wang, Y.P. Wang, Z.L. Jiang, Test technology of longitudinal stage separation for two-stage-to-orbit vehicle in shock tunnel, Acta Aeronautica Astronautica Sinica 44 (2023) 128126 (in Chinese).

[25] Y. Wang, Y.P. Wang, Z.L. Jiang, Experimental and numerical investigation on the unsteady interaction in longitudinal stage separation for parallel-staged two-body configuration, Phys. Fluids 36 (2024) 016116.

[26] J.P. Decker, Aerodynamic Interference Effects Caused by Parallel-Staged Simple Aerodynamic Configurations at Mach Numbers of 3 and 6, Report No. NASA-TN-D-5379, NASA, 1969.

[27] W. Bordelon, A. Frost, D. Reed, Stage separation wind tunnel tests of a generic TSTO launch vehicle, in: 21st AIAA Applied Aerodynamics Conference, AIAA Paper 20003-4227, 2003.

[28] H. Ozawa, K. Kitamura, K. Hanai, K. Mori, Y. Nakamura, Unsteady aerodynamic interaction between two bodies at hypersonic speed, Trans. Jpn. Soc. Aeronaut. Space Sci. 53 (2010) 114–121.

[29] T. Uematsu, S. Aso, Y. Tani, Aerodynamic interference reduction method for two-stage launch vehicles supersonic separation, in: 49th AIAA Aerospace Sciences Meeting Including the New Horizons Forum and Aerospace Exposition, AIAA Paper 2011-388, 2011.

[30] J. Cheng, R. Chen, R. Qiu, W. Sun, Y. You, Aerothermodynamic study of two-stage-to-orbit system composed of wide-speed range vehicle and rocket, Acta Astronaut. 183 (2021) 330–345.

[31] P. Liao, J. Chu, W. Song, Y. Zhang, Unsteady investigation on parallel separation for spiked two-stage reusable launch vehicle, Chin. J. Aeronaut. (2023), https://doi.org/10.1016/j.cja.2023.11.020 (In Press).

[32] Y. Wang, Y.P. Wang, X.P. Xue, Z.L. Jiang, Numerical investigation on safe stage separation problem of a TSTO model at Mach 7, Chin. J. Theor. Appl. Mech. 54 (2022) 526–542 (in Chinese).

[33] T. Cvrlje, Unsteady separation of a two-stage hypersonic vehicle, in: 30th Fluid Dynamics Conference, AIAA Paper No. AIAA-99-3412, 1999.

[34] T. Cvrlje, C. Breitsamter, B. Laschka, Numerical simulation of the lateral aerodynamics of an orbital stage at stage separation flow conditions, Aero. Sci. Technol. 4 (2000) 157–171.

[35] M.A. Moelyadi, C. Breitsamter, B. Laschka, Stage-separation aerodynamics of two-stage space transport systems Part1: steady-state simulations, J. Spacecraft Rockets 45 (2008) 1230–1239.

[36] M.A. Moelyadi, C. Breitsamter, B. Laschka, Stage-separation aerodynamics of two-stage space transport systems Part 2: unsteady simulation, J. Spacecraft Rockets 45 (2008) 1240–1250.

[37] Y. Liu, Z.S. Qian, W. Lu, S. He, Numerical investigation on the safe stage-separation mode for a TSTO vehicle, Aero. Sci. Technol. 107 (2020) 106349.

[38] S. Chakravarthy, A unified-grid finite volume formulation for computational fluid dynamics, Int. J. Numer. Methods Fluid. 31 (1999) 309–323.

[39] E.F. Toro, Riemann Solvers and Numerical Methods for Fluid Dynamics: a Practical Introduction, Springer Science & Business Media, New York, 2009.

[40] H. Luo, J. Baum, R. Lohner, Extension of HLLC scheme for flows at all speeds, in: 16th AIAA Computational Fluid Dynamics Conference, AIAA Paper No. AIAA 2003-3840, 2003.

[41] J.R. Edwards, An implicit multi-grid algorithm for computing hypersonic, chemically reacting viscous flows, J. Comput. Phys. 123 (1996) 84–95.

[42] M.K. Liu, G.L. Han, Z.L. Jiang, Experimental study on the evolution of mode waves in laminar boundary layer on a large-scale flat plate, Phys. Fluids 34 (2022) 013612.

[43] M.K. Liu, G.L. Han, Z.L. Jiang, Experimental study on the effects of the cone nose-tip bluntness, Phys. Fluids 34 (2022) 101703.
[44] W. Schroder, G. Hartmann, Analysis of inviscid and viscous hypersonic flows past a two-stage spacecraft, J. Spacecraft Rockets 30 (1993) 8–13.
[45] W. Schroder, F. Mergler, Investigation of the flowfield over parallel-arranged launch vehicles, in: 23rd Fluid Dynamics, Plasmadynamics, And Lasers Conference, AIAA Paper No. AIAA 93-3060, 1993.
[46] Z.H. Wang, Theoretical Modelling of Aeroheating on Sharpened Noses under Rarefied Gas Effects and Non-equilibrium Real Gas Effects, Springer Thesis, Beijing, 2014.
[47] Y.B. Gan, A.G. Xu, G.C. Zhang, Y.D. Zhang, S. Succi, Discrete Boltzmann trans-scale modeling of high-speed compressible flows, Phys. Rev. 97 (2018) 053312.
[48] S.L. Tian, J.W. Fu, J.T. Chen, A numerical method for multibody separation with collisions, Aero. Sci. Technol. 109 (2021) 106426.
[49] M.S. Holden, M. MacLean, T.P. Wadhams, A. Dufrene, Measurements of real gas effects on regions of laminar shock wave/boundary layer interaction in hypervelocity flows for "Blind" code validation studies, in: 21st AIAA Computational Fluid Dynamics Conference, AIAA Paper No. AIAA 2013-2837, 2013.
[50] R.R. Heim, CFD Wing/pylon/finned Store Mutual Interference Wind Tunnel Experiment, Report No. AEDC-TSR-91-P4, NASA, 1991.
[51] D. Snyder, E. Koutsavdis, J. Anttonen, Transonic store separation using unstructured CFD with dynamic meshing, in: 33rd AIAA Fluid Dynamics Conference and Exhibit, AIAA Paper No. AIAA 2003-3919, 2003.
[52] C.Q. Liu, Y.S. Gao, S.L. Tian, X.R. Dong, Rortex—a new vortex vector definition and vorticity tensor and vector decompositions, Phys. Fluids 30 (2018) 035103.
[53] Y.S. Gao, C.Q. Liu, Rortex and comparison with eigenvalue-based vortex identification criteria, Phys. Fluids 30 (2018) 085107.
[54] B.N. Pamadi, Performance, Stability, Dynamics, and Control of Airplanes, American Institute of Aeronautics and Astronautics, America, 2015.
[55] J.D. Anderson, Fundamentals of Aerodynamics, Mc Graw Hill, America, 2010.
[56] A. Viviani, G. Pezzella, Aerodynamic and Aerothermodynamic Analysis of Space Mission Vehicles, Springer, Switzerland, 2015.